Journal of Sound and Vibration 621 (2026) 119482

Contents lists available at ScienceDirect

Journal of Sound and Vibration

journal homepage: www.elsevier.com/locate/jsvi

Rayleigh waves guided by elastic metasurfaces coupled to a resonant half-space

Farhad Zeighami [a,*], Antonio Palermo [a], Parisa Shokouhi [b], Alessandro Marzani [a]

[a] Department of Civil, Chemical, Environmental and Materials Engineering - DICAM, University of Bologna, Viale Risorgimento, 2, Bologna, 40136, Italy

[b] Department of Engineering Science and Mechanics, The Pennsylvania State University, University Park, 16802, USA

ARTICLE INFO

Keywords:
Rayleigh waves
Locally resonant metamaterials
Elastic metasurfaces
Wave guiding
Wave filtering
Dispersion relation

ABSTRACT

Controlling the propagation of surface Rayleigh waves along complex geometries is essential for advanced engineering applications, including seismic wave mitigation, ultrasonic nondestructive testing, and surface acoustic wave technologies. However, energy leakage and scattering remain significant obstacles for this purpose. This paper discusses how resonant metamaterials can be used to guide Rayleigh waves along a non-flat irregular surface while minimizing scattering and energy loss in the bulk. This objective is achieved by designing an elastic metasurface of mass–spring oscillators, coupled to a resonant half-space constructed from several rows of periodically embedded mechanical resonators. In this framework, the metasurface is treated as a resonant boundary condition, whereas the resonant half-space is modeled as an equivalent homogenized medium characterized by effective mechanical parameters thanks to a dedicated homogenization technique. The sub-wavelength dimension for both surface and embedded resonators allows the derivation of a closed-form dispersion law.

The dispersion analysis reveals the hybridization of the fundamental surface mode around the resonance frequency of the half-space, leading to the formation of a low-frequency bandgap. When the resonance frequency of the metasurface is tuned to fall within the bandgap frequency range, a highly confined and slow-moving surface mode emerges. This mode enables effective guidance of Rayleigh waves along surfaces with complex and irregular geometries. By tailoring the metasurface design, surface wave transmission can be optimized, while issues such as leakage and scattering at discontinuities are mitigated. This approach advances surface wave manipulation, offering promising implications for a wide range of engineering applications.

1. Introduction

Rayleigh waves (RW) are a specific type of elastic waves that travel along the surface of a semi-infinite solid, with their velocity determined by the elastic moduli and density of the medium [1]. These waves exhibit a displacement field with both longitudinal and shear components, resulting in an elliptical particle motion. Rayleigh waves are of interest for a wide range of applications across various frequency ranges: from seismology at Hz to nondestructive testing and surface acoustic wave devices at kHz, and sensors at MHz range [2].

* Corresponding author.
E-mail address: farhad.zeighami3@unibo.it (F. Zeighami).

https://doi.org/10.1016/j.jsv.2025.119482
Received 26 March 2025; Received in revised form 27 September 2025; Accepted 30 September 2025
Available online 4 October 2025
0022-460X/© 2025 The Authors. Published by Elsevier Ltd. This is an open access article under the CC BY license (http://creativecommons.org/licenses/by/4.0/).

Recently, elastodynamic metamaterials have been proposed to manipulate surface wave propagation on different frequency scales. Elastodynamic metamaterials rely on various mechanisms, including Bragg scattering, local resonance, and inertial amplification, to manipulate waves across different wavelength scales. Bragg scattering originates from periodic variations in material properties or geometry, leading to destructive interference when the wavelength is comparable to the lattice spacing. This mechanism, first explored in phononic crystals [3,4], typically produces wide bandgaps at relatively high frequencies determined by structural periodicity, in which wave propagation is inhibited. In contrast, the local resonance mechanism exploits resonators embedded or attached to a host medium to induce bandgaps well below the Bragg limit. This concept, pioneered by Liu et al. [5] and further developed in various configurations [6,7], enables wave attenuation and manipulation in the sub-wavelength regime, offering greater flexibility for low-frequency applications. The inertial amplification mechanism, on the other hand, employs mechanical linkages to amplify the relative motion between components, thereby increasing the effective inertia of the system and allowing the generation of wider bandgaps without the need for large added masses [8]. Among different types of elastic metematerials, locally resonant metamaterials (LRMs) exploit local resonance mechanisms to design sub-wavelength resonant units capable of creating narrow frequency bandgaps. Thanks to their capability to open low-frequency bandgaps, LRMs have demonstrated broad applicability in multiple scientific fields, including mechanics and civil engineering [9,10].

To date, most studies on the interaction between surface waves and LRMs have focused on elastic resonant metasurfaces, which are thin resonant layers attached to the surface of an elastic waveguide. These interfaces are typically constructed using arrays of sub-wavelength discrete oscillators, such as mass–spring-dashpot systems [11], plates/beams [12,13], and pillars [14,15]. Compared to phononic crystals or bulk LRMs, elastic resonant metasurfaces integrate resonant units within a single surface layer, enabling compact designs with reduced fabrication complexity and precise phase–amplitude control for wavefront shaping without altering the bulk medium. Leveraging the elliptical particle motion of surface Rayleigh waves to activate their resonant units, elastic resonant metasurfaces provide an efficient design for passive control of surface waves, generating narrow and tunable low-frequency bandgaps [16]. Other notable frequency-specific applications of LRMs include seismic isolation devices [11,17–19], railway vibration mitigation systems [20,21], energy harvesting [22,23], non-destructive testing [24], fluid-solid interaction [25], and surface acoustic wave devices [26].

A more recent concept to control surface wave propagation involves the use of thick LRM layers [27]. In this approach, mechanical resonators are embedded within the depth of the host material. Unlike elastic metasurfaces, the resonant layer has a thickness comparable to the wavelength of incoming surface waves. The interaction between Rayleigh waves and the thick LRM layer results in the formation of leaky surface waves, which radiate a portion of the wave energy into the bulk of the material. This leads to a wider spectral bandgap and improved filtering capabilities for surface waves [28].

The interaction between Rayleigh waves and architected surfaces could disrupt wave energy transmission and lead to scattering and reflection depending on variations in surface topography [29]. So far, several studies have explored the possibility of guiding surface Rayleigh waves along the horizontal plane. For example, elastic metasurfaces have been used to channel surface waves along terraced slopes [30], while gradient-index lenses have been designed to steer surface wave energy [31]. More recently, broadband cloaks have been proposed to reroute these waves around surface defects, effectively rendering them invisible and enabling wave guiding in vertical (i.e., sagittal) planes, those containing both the propagation (x) and polarization (z) directions [32]. However, cloaking techniques often require material with unfeasible constitutive properties, e.g. symmetry breaking, which limits their practical implementation. To address this challenge, this study proposes the use of LRMs to enable efficient and robust guiding of Rayleigh waves along surfaces with vertical irregular geometries.

The proposed wave guiding approach combines a resonant half-space consisting of a periodic arrangement of multiple rows of embedded mechanical resonators with elastic metasurfaces attached to its free surface. This configuration represents an advancement over previous works (e.g., Ref. [27]), where the focus was primarily on the interaction of a resonant half-space and Rayleigh waves. Here, the introduction of elastic metasurfaces enables the coupling of surface modes and allows controlled wave guidance along engineered paths. To this end, a homogenization technique is used to estimate the effective mechanical parameters of the resonant half-space. These parameters are essential for deriving an analytical dispersion law that characterizes Rayleigh wave propagation in an equivalent homogenized model of the half-space. The elastic metasurfaces are then modeled as a resonance boundary condition that exerts a uniform stress on the surface of the waveguide [33]. By properly tuning the mechanical parameters of the metasurfaces, a highly localized surface mode is generated around the collective resonance frequency of the metasurfaces in the dispersion relation, enabling effective guidance of waves along surfaces with irregular topography. The efficiency of this method is demonstrated through multiple case studies and validated using results of finite element (FE) modeling and simulations.

This paper is organized as follows: Section 2 presents the analytical model used to derive the dispersion law. Section 3 provides a detailed discussion on the numerical analysis of the dispersion relations. The wave guiding application is explored in Section 4. Finally, Section 5 concludes the paper with a summary of the key findings.

2. Analytical dispersion relation of elastic metasurfaces attached to the surface of a resonant half-space

The investigation begins by examining the dispersive properties of Rayleigh-like surface waves propagating along a resonant half-space coupled with an array of sub-wavelength mass–spring oscillators, as shown in Fig. 1(a). For the sake of simplicity, the analysis is limited to RWs propagating within the x-z plane under plane-strain conditions.

The resonant half-space includes mechanical resonators embedded within a host material characterized by isotropic, homogeneous, and elastic properties, denoted by ρ_{h}, $c_{L,\mathrm{h}}$, and $c_{T,\mathrm{h}}$ for mass density, longitudinal, and transverse (shear) bulk wave velocities, respectively. The embedded resonators are periodically arranged in square lattice structures to form the resonant half-space. The

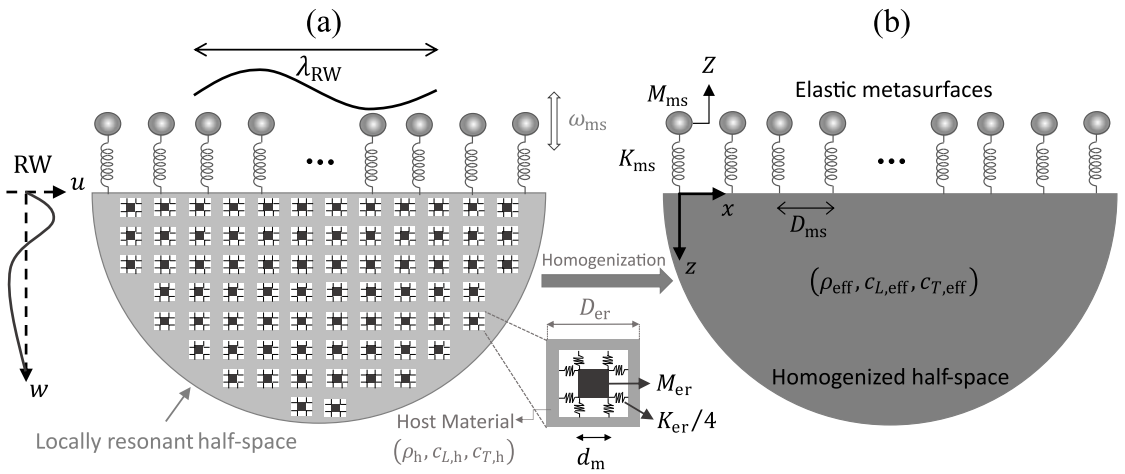

Fig. 1. (a) Schematic of elastic metasurfaces attached to the surface of a resonant half-space made of embedded mechanical resonators. The inset shows the fundamental unit cell of the resonant half-space. (b) Elastic metasurfaces attached to the surface of the equivalent homogenized half-space characterized by effective mechanical properties.

2D unit cell of the lattice has a length D_{er} and includes a rigid square internal mass (M_{er}) with a dimension of $D_m = 0.5\, D_{er}$, as shown in the inset of Fig. 1(a). The internal mass is suspended within the host material by horizontal and vertical elastic springs, each having a length of $0.1\, D_{er}$ and identical axial stiffness. This configuration results in two resonant modes with an equal angular frequency $\omega_{er,x} = \omega_{er,z} = \omega_{er}$ along the principal axes x and z, where $\omega_{er} = \sqrt{K_{er}/M_{er}}$, and K_{er} is the overall stiffness in each axis. In the long-wavelength regime, these resonators have dimensions significantly smaller than the wavelength of the Rayleigh waves ($D_{er} \ll \lambda_{RW}$), thereby allowing them to be modeled as a homogenized composite material.

2.1. Effective medium description of the resonant half-space

A homogenization technique is used to describe the resonant half-space as an equivalent homogeneous and isotropic medium (see Fig. 1(b)) characterized by an effective mass density, $\rho_{eff}(\omega)$, and effective bulk wave velocities ($c_{L,eff}(\omega)$ and $c_{T,eff}(\omega)$) [27]. The effective mass density of the homogenized composite material is estimated according to the frequency-dependent function [34]:

$$\rho_{eff}(\omega) = \rho_{st}\left(1 + \rho_0 \frac{\omega^2}{\omega_{er}^2 - \omega^2}\right), \tag{1}$$

where $\rho_{st} = \rho_h + \rho_{er}$ is the static density obtained at $\omega = 0$, ρ_{er} is the mass density of the embedded resonators, and $\rho_0 = \rho_{er}/\rho_{st}$ represents the ratio between the mass density of the embedded resonators to the static density. The adopted homogenization approach assumes that the wavelength is much larger than both the spacing and size of the embedded resonators and remains valid for a random distribution of resonators.

The effective bulk velocities of the resonant half-space are determined through a static homogenization approach, as detailed in Ref. [27]:

$$c_{L,eff}(\omega) = \sqrt{\frac{M_{eff}}{\rho_{eff}(\omega)}}, \quad c_{T,eff}(\omega) = \sqrt{\frac{\mu_{eff}}{\rho_{eff}(\omega)}}, \tag{2}$$

where M_{eff} and μ_{eff} represent the effective longitudinal and shear moduli of the composite, respectively. Their derivations are provided in Appendix A.

2.2. Derivation of the dispersion relation

Consider plane harmonic waves propagating with angular frequency ω and wavenumber k, traveling along the surface of the homogenized half-space in the horizontal direction (x-axis). For a wave polarized in the $x-z$ plane, the horizontal (u) and vertical (w) displacement components of the homogenized LRM half-space can be expressed as follows after omitting the common propagating term $\exp(\mathrm{i}(\omega t - kx))$:

$$\begin{aligned} u(z) &= -k\,(A\,\mathrm{i}\,\exp(-k\alpha z) - B\,\beta\,\exp(-k\beta z)), \\ w(z) &= -k\,(A\,\alpha\,\exp(-k\alpha z) + B\,\mathrm{i}\,\exp(-k\beta z)), \end{aligned} \tag{3}$$

where A and B denote the two unknown amplitudes of the body waves, and α and β are defined as [35]:

$$\alpha(k,\omega)=\sqrt{1-\frac{\omega^2}{k^2c_{L,\mathrm{eff}}^2(\omega)}},\quad \beta(k,\omega)=\sqrt{1-\frac{\omega^2}{k^2c_{T,\mathrm{eff}}^2(\omega)}}. \tag{4}$$

The surface Rayleigh waves exhibit an exponentially decaying profile in z. This property holds if the wave velocity $c=\omega/k$ along the surface of the resonant half-space satisfies the condition $c<c_{T,\mathrm{eff}}<c_{L,\mathrm{eff}}$.

From linear elastic (isotropic) constitutive relations, the normal (σ_{zz}) and tangential (σ_{zx}) stress components are derived as:

$$\begin{aligned}\sigma_{zz}(z,k,\omega)&=\rho_{\mathrm{eff}}(\omega)(\delta A\,\exp(-k\alpha z)+\mathrm{i}\,\gamma\,\beta\,B\,\exp(-k\beta z))\,\omega^2,\\ \sigma_{zx}(z,k,\omega)&=\rho_{\mathrm{eff}}(\omega)(\mathrm{i}\,\alpha\,\gamma\,A\,\exp(-k\alpha z)-\delta B\,\exp(-k\beta z))\,\omega^2,\end{aligned} \tag{5}$$

where $\gamma(k,\omega)=2\left(kc_{T,\mathrm{eff}}/\omega\right)^2$ and $\delta(k,\omega)=\gamma(k,\omega)-1$.

At this stage, an effective medium approach is used to account for the presence of surface oscillators [36]. According to this approach, the sub-wavelength dimension of single-degree-of-freedom oscillators enables the metasurface to be modeled as a resonant boundary condition which exerts a uniform normal stress on the surface of the half-space [33]. The exerted normal stress is approximated as:

$$\sigma_{zz,\mathrm{ms}}(z=0,k,\omega)=\frac{M_{\mathrm{ms}}\omega_{\mathrm{ms}}^2}{S_{\mathrm{ms}}}\left(\frac{\omega^2}{\omega^2-\omega_{\mathrm{ms}}^2}\right)w(z=0)=\bar{\sigma}_{zz,\mathrm{ms}}, \tag{6}$$

where $\bar{\sigma}_{zz,\mathrm{ms}}$ is the mean normal stress for a generic distribution of n_{ms} surface oscillators, $\omega_{\mathrm{ms}}=\sqrt{K_{\mathrm{ms}}/M_{\mathrm{ms}}}$ is the angular resonance frequency of the oscillators, M_{ms} is the total inertia, K_{ms} is the spring stiffness of the oscillators, $S_{\mathrm{ms}}=D_{\mathrm{ms}}^2$ is their influence surface area, and $w(z=0)$ is the vertical base displacement of the oscillators at their junction with the surface of the half-space. The effective medium description of elastic metasurfaces captures the averaged dynamic response of the array of resonators and remains valid when the dimensions of the surface oscillators are much smaller than the characteristic wavelength of surface waves [36], even if the mechanical oscillators are not arranged regularly within the metasurface array. This approach ensures that the specific lattice symmetry of the oscillators does not introduce any directional effects on the dispersive properties of the coupled resonant system.

By imposing the following boundary conditions:

$$\sigma_{zz}(z=0,k,\omega)=\bar{\sigma}_{zz,\mathrm{ms}},\quad \sigma_{zx}(z=0,k,\omega)=0, \tag{7}$$

namely, continuity of normal stresses and null tangential stress at the interface between the metasurface and resonant half-space, a dispersion relation is derived. These two boundary conditions yield a system of two homogeneous equations given in matrix form as:

$$\begin{bmatrix} 2\mathrm{i}\sqrt{1-\left(\frac{\omega}{kc_{L,\mathrm{eff}}}\right)^2} & 2-\left(\frac{\omega}{kc_{T,\mathrm{eff}}}\right)^2-\frac{M_{\mathrm{ms}}\omega_{\mathrm{ms}}^2\sqrt{1-\left(\frac{\omega}{kc_{L,\mathrm{eff}}}\right)^2}}{S_{\mathrm{ms}}c_{T,\mathrm{eff}}^2\rho_{\mathrm{eff}}k}\left(\frac{\omega^2}{\omega^2-\omega_{\mathrm{ms}}^2}\right) \\ 2-\left(\frac{\omega}{kc_{T,\mathrm{eff}}}\right)^2 & 2\mathrm{i}\sqrt{1-\left(\frac{\omega}{kc_{T,\mathrm{eff}}}\right)^2}+\mathrm{i}\,\frac{M_{\mathrm{ms}}\omega_{\mathrm{ms}}^2}{S_{\mathrm{ms}}c_{T,\mathrm{eff}}^2\rho_{\mathrm{eff}}k}\left(\frac{\omega^2}{\omega^2-\omega_{\mathrm{ms}}^2}\right)\end{bmatrix}\begin{bmatrix}A\\B\end{bmatrix}=\begin{bmatrix}0\\0\end{bmatrix}. \tag{8}$$

Eq. (8) can be compactly written as $\mathbf{D}(k,\omega)\mathbf{A}=\mathbf{0}$. Imposing $\det(\mathbf{D}(k,\omega))=0$ yields a closed-form dispersion law:

$$\left(\frac{\omega^2}{\omega_{\mathrm{ms}}^2}-1\right)\left[\left(2-\left(\frac{\omega}{kc_{T,\mathrm{eff}}}\right)^2\right)^2-4\sqrt{1-\left(\frac{\omega}{kc_{T,\mathrm{eff}}}\right)^2}\sqrt{1-\left(\frac{\omega}{kc_{L,\mathrm{eff}}}\right)^2}\right]=\frac{M_{\mathrm{ms}}\omega^4}{S_{\mathrm{ms}}\rho_{\mathrm{eff}}c_{T,\mathrm{eff}}^4k^3}\sqrt{1-\left(\frac{\omega}{kc_{L,\mathrm{eff}}}\right)^2}. \tag{9}$$

Eq. (9) reduces to the dispersion relation for Rayleigh waves propagating in an elastic metasurface attached to the surface of an isotropic and homogeneous half-space when the LRM is replaced by the host material, with $\rho_{\mathrm{eff}}=\rho_{\mathrm{h}}$, $c_{L,\mathrm{eff}}=c_{L,\mathrm{h}}$, and $c_{T,\mathrm{eff}}=c_{T,\mathrm{h}}$ [16]. If the mass of the metasurface vanishes ($M_{\mathrm{ms}}=0$), the dispersion relation recovers that of Rayleigh waves traveling in a resonant half-space [27]. If both the embedded and surface resonator masses are zero ($M_{\mathrm{er}}=M_{\mathrm{ms}}=0$), the effective mechanical parameters of the resonant half-space match those of the host material. As a result, Eq. (9) reverts to the classical dispersion relation for Rayleigh waves [1].

3. Numerical analysis of dispersion relations

This section discusses three case studies that illustrate different possible interactions between the metasurface and the resonant half-space. In Case I, the metasurface resonance frequency is set equal to that of the resonant half-space, and the coupling of their resonant behaviors leads to an extended bandgap. Case II examines a metasurface with resonance frequencies outside the bandgap, highlighting the effects of off-resonant coupling. In Case III, the metasurface resonance frequency lies within the bandgap of the resonant half-space, demonstrating the potential for enhanced surface wave confinement and reduced leakage in the bulk. For clarity, all geometric and mechanical parameters are normalized as follows:

- normalized coordinates : $\hat{x}=xk_0$, $\hat{z}=zk_0$, with $k_0=\frac{\pi}{D_{\mathrm{er}}}$;
- normalized densities and mass: $\hat{\rho}_{\mathrm{h}}=\frac{\rho_{\mathrm{h}}}{\rho_{\mathrm{st}}}$, $\hat{\rho}_{\mathrm{er}}=\frac{\rho_{\mathrm{er}}}{\rho_{\mathrm{st}}}$, $\hat{\rho}_{\mathrm{eff}}=\frac{\rho_{\mathrm{eff}}}{\rho_{\mathrm{st}}}$, $\hat{M}_{\mathrm{ms}}=\frac{M_{\mathrm{ms}}k_0}{S_{\mathrm{ms}}\rho_{\mathrm{st}}}$;
- frequency and wavenumber: $\hat{\omega}=\frac{\omega}{\omega_{\mathrm{er}}}$, $\hat{\omega}_{\mathrm{ms}}=\frac{\omega_{\mathrm{ms}}}{\omega_{\mathrm{er}}}$, $\hat{k}=\frac{k}{k_0}$;

Table 1
Normalized parameters of the system used in the numerical analysis.

Symbol	Definition	Value
$\hat{D}_{\text{er}}$	Lattice constant	π
$\hat{\lambda}_{\text{ref}}$	Reference wavelength	8.02
$\hat{\rho}_{\text{h}}$	Mass density of the host material	0.96
$\hat{\rho}_{\text{er}}$	Mass density of the embedded resonators	1.54
$\hat{c}_{T,\text{h}}$	Shear bulk wave speed in the host material	1
$\hat{c}_{L,\text{h}}$	Longitudinal bulk wave speed in the host material	2.8
$\hat{\omega}_{\text{er}}$	Angular resonance frequency of the embedded resonators	1
$\hat{D}_{\text{ms}}$	Lattice distance between the surface oscillators	π
$\hat{\omega}_{\text{ms}}$	Angular resonance frequency of the metasurface	var.

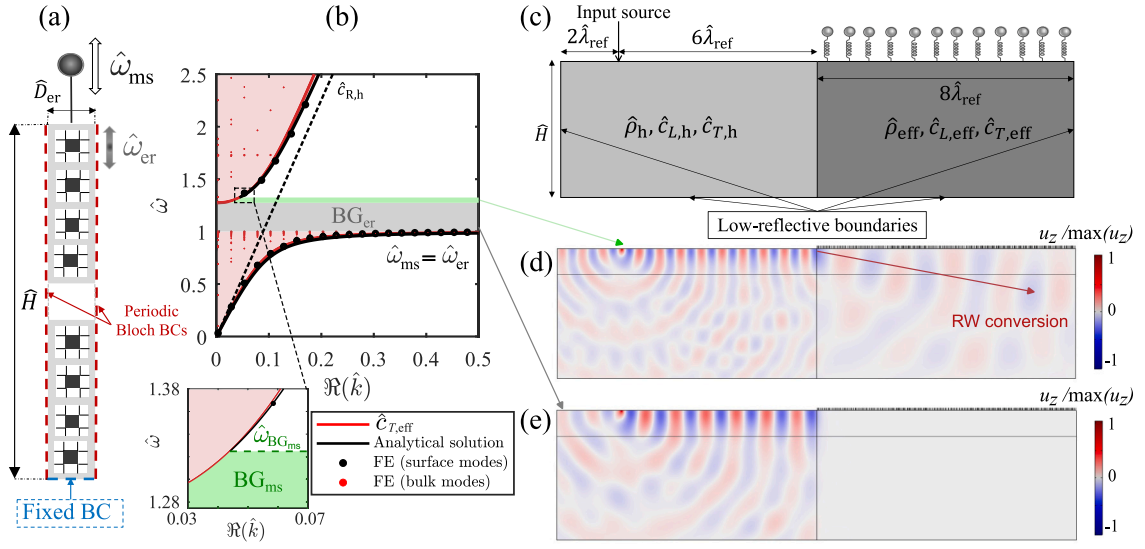

Fig. 2. (a) Schematics of the resonant column used to calculate the numerical dispersion relation. (b) Dispersion relation of Case I: a resonant half-space equipped with a resonant metasurface with identical resonance frequencies ($\hat{\omega}_{\text{ms}} = \hat{\omega}_{\text{er}}$). The inset shows the bandgap extension (highlighted green region) due to the presence of the metasurface. (c) Schematic of the full 2D FE model. The vertical displacement wavefields for (d) $\hat{\omega}^* = 1.32$ and (e) $\hat{\omega}^* = 1.1$, showcasing surface wave conversion and attenuation, respectively. (For interpretation of the references to color in this figure legend, the reader is referred to the web version of this article.)

- normalized wavelength and lengths: $\hat{\lambda}_{\text{ref}} = \frac{\lambda_{\text{ref}}}{k_0} = \frac{2\pi c_{T,\text{h}}}{\omega_{\text{er}} k_0}$, $\hat{D}_{\text{er}} = D_{\text{er}} k_0$, $\hat{D}_{\text{ms}} = \hat{D}_{\text{er}}$;
- velocities: $\hat{c}_{L,\text{h}} = \frac{c_{L,\text{h}}}{c_{T,\text{h}}}$, $\hat{c}_{T,\text{h}} = \frac{c_{T,\text{h}}}{c_{T,\text{h}}}$, $\hat{c}_{L,\text{eff}} = \frac{c_{L,\text{eff}}}{c_{T,\text{h}}}$, $\hat{c}_{T,\text{eff}} = \frac{c_{T,\text{eff}}}{c_{T,\text{h}}}$, $\hat{c}_{R,\text{eff}} = \frac{c_{R,\text{eff}}}{c_{T,\text{h}}}$.

The chosen normalized values are provided in Table 1:

3.1. Case I: equal resonance frequencies, $\hat{\omega}_{\text{ms}} = \hat{\omega}_{\text{er}}$

This configuration is achieved by setting the inertia and total stiffness of the metasurface equal to those of the embedded resonators, that is, $\hat{M}_{\text{ms}} = \hat{M}_{\text{er}}$ and $\hat{K}_{\text{ms}} = \hat{K}_{\text{er}}$, which results in $\hat{\omega}_{\text{ms}} = \hat{\omega}_{\text{er}}$. The dispersion relation is determined by calculating the effective mass density and the bulk speeds of the homogenized material (details provided in Appendix A) and solving Eq. (9) numerically using the parameters listed in Table 1. The values of $\hat{\omega}$ are used as input, and the complex dimensionless wavenumbers $\hat{k}$ are computed using the Newton–Raphson root-finding method.

Fig. 2(b) presents the dispersion curve for real values of the dimensionless wavenumber. This case study shows dispersive behavior similar to that of a resonant half-space without metasurfaces, as reported in [27]. Two regions, highlighted in red, are identified by the effective shear velocity (represented by solid red lines), indicating areas where only bulk waves can propagate. The fundamental surface mode splits into two branches, denoted by solid black lines, leading to the formation of a bandgap within the range $\hat{\omega}_{\text{BG}_{\text{er}}} = [1, \hat{\omega}_{\text{zd}}]$ as highlighted in gray in Fig. 2(b), where $\hat{\omega}_{\text{zd}} = 1/\sqrt{1-\rho_0} = 1.27$ is the zero-density frequency (see Fig. A.2(a) for details). This bandgap corresponds to the one associated with bulk waves, as observed in Fig. A.2(c). The lower branch of the fundamental surface mode propagates with a phase velocity close to the Rayleigh velocity of the host material ($\hat{c}_{R,\text{h}}$), shown by the dashed black line, at very low frequencies, and asymptotically approaches the resonance, $\hat{\omega}_{\text{er}} = \hat{\omega}_{\text{ms}}$.

The upper branch begins to propagate from the upper edge of the bandgap and gradually approaches the Rayleigh velocity of the host material at higher frequencies. The metasurface contributes to the extension of the bulk wave bandgap, indicated as a light green region in Fig. 2(b), due to its strong coupling with surface waves at resonance. The overall bandgap range, determined by superposition of the bandgaps generated by the two resonant systems, is $\hat{\omega}_{\mathrm{BG}} = [1, \hat{\omega}_{\mathrm{BG_{ms}}}]$, where $\hat{\omega}_{\mathrm{BG_{ms}}} = \hat{\omega}_{\mathrm{zd}} + B_{\mathrm{ms}} + \sqrt{B_{\mathrm{ms}}^2 + 1} - 1 = 1.32$, in which the metasurface bandgap coefficient B_{ms} is defined as [11]:

$$B_{\mathrm{ms}} = \frac{M_{\mathrm{ms}}\ \omega_{\mathrm{ms}}}{2 S_{\mathrm{ms}}\ \rho_{\mathrm{h}}\ c_{T,\mathrm{h}}} \sqrt{1 - \left(\frac{c_{T,\mathrm{h}}}{c_{L,\mathrm{h}}}\right)^2} = 0.15. \tag{10}$$

To validate these findings, a numerical FE model is developed in COMSOL Multiphysics [37] under plane-strain conditions using the wave finite element approach initially introduced in Ref. [38] and adapted for surface Rayleigh waves interacting with embedded LRMs [27,28]. The FE model is constructed by periodically distributing the basic cell shown in the inset of Fig. 1(a) on a regular grid with a lattice constant of $\hat{D}_{\mathrm{er}}$ along the vertical ($\hat{z}$) direction, resulting in a locally resonant column with a total height of $\hat{H} = 3\,\hat{\lambda}_{\mathrm{ref}}$, as shown schematically in Fig. 2(a). The column height is selected to be sufficiently large so that the exponentially decaying surface wave energy vanishes before reaching the bottom boundary. This approach is commonly adopted in surface wave simulations for its simplicity and computational efficiency, particularly when surface confinement dominates and bottom reflections are negligible [39]. The internal resonating mass and host material are modeled as linear-elastic solid elements, whereas their connection by elastic springs are represented via truss elements. Lagrange quadrilateral elements are used to discretize the solid parts, with a mesh size ranging from $\hat{D}_{\mathrm{er}}/10$ to $\hat{D}_{\mathrm{er}}$ as minimum and maximum values, while the springs are discretized with a single-element mesh. The bottom edge of the FE model is restrained in both directions to prevent any undesired rigid body motion, and periodic Bloch boundary conditions are applied at the side edges in the x-direction to account for periodicity. The metasurface is modeled by a 2D truss element: a tip mass is added to the truss, with its displacement constrained in the horizontal direction to capture only the vertical longitudinal mode of the surface-mounted resonator.

By sweeping the dimensionless wavenumber in the range $\hat{k} = [0, 1]$, the dimensionless eigenfrequencies of the FE model are calculated and superimposed on the analytical dispersion curves shown in Fig. 2(b). The FE eigensolutions predict a mix of bulk and surface modes. The Classification Mode Criterion (*CMC*) is employed to identify surface modes based on the position of the displacement shape centroid [27]:

$$CMC = \frac{\int_0^{\hat{H}} |\hat{w}|\,\hat{z}\,\mathrm{d}\hat{z}}{\int_0^{\hat{H}} |\hat{w}|\,\mathrm{d}\hat{z}} < 0.9\,\hat{\lambda}_{\mathrm{ref}}, \tag{11}$$

where $\hat{w}$ is the vertical nodal displacement. This criterion selects modes with a displacement centroid confined to the uppermost part of the model depth and identifies them as surface modes. In Fig. 2(b), bulk modes are represented by red dots, while the surface modes are shown by black dots. Notably, a good agreement between the analytical surface modes (shown as black solid lines) and the FE solutions (black dots) is obtained.

To further investigate the wave propagation characteristics, harmonic analysis is performed on a full 2D FE model with a height of $\hat{H}$ and an overall length of $2\hat{L}_{\mathrm{m}}$, as shown schematically in Fig. 2(c). The model is divided into two sections of equal length ($\hat{L}_{\mathrm{m}} = 8\,\hat{\lambda}_{\mathrm{ref}}$): (i) the reference part, consisting of the host material, where the input source (a unitary vertical displacement point source) excites the model, and (ii) the LRM part, characterized by an equivalent homogenized resonant material with metasurfaces on top. The input source is placed at a distance of $2\,\hat{\lambda}_{\mathrm{ref}}$ from the left corner of the model to ensure proper surface wave propagation before reaching the metamaterial section. A buffer zone of $6\,\hat{\lambda}_{\mathrm{ref}}$ is placed between the source and the LRM part to mitigate the near-source effects. Low-reflective boundary conditions are applied along the lateral and bottom edges of the model to minimize unwanted wave reflections from the boundaries. Since the elastic wave energy is primarily confined to the surface part of the model, a portion with a height of $\hat{H}/5$ is discretized with a finer mesh, having a maximum dimension of $\hat{D}_{\mathrm{er}}/5$.

The numerical model is initially excited at a frequency within the bandgap of the resonant half-space, $\hat{\omega}^* = 1.1$. The vertical displacement wavefield, shown in Fig. 2(e), confirms that surface waves are entirely attenuated in the LRM part. This occurs because the elastic wave energy is dissipated through the strong coupling between the motion of the embedded resonators and the surface waves. Next, the model is excited at a frequency within the secondary bandgap induced by the metasurfaces ($\hat{\omega}^* = 1.32$), as shown in Fig. 2(d). In this frequency range, where $\hat{c} < \hat{c}_{T,\mathrm{eff}}$, the dynamic response of the resonant system is governed by the metasurface, which inhibits surface waves and allows only bulk waves to propagate. As a result, when surface waves reach the LRM zone, surface-to-shear wave conversion occurs, causing the wave trajectory to deviate from the surface into the bulk of the homogenized composite material. This wave conversion, which provides an additional filtering property for the system, has been observed in previous studies on the interaction between surface waves and metasurfaces located on top of an isotropic and homogeneous half-space [11,14].

3.2. Case II: metasurface resonance frequency outside the half-space bandgap $\hat{\omega}_{\mathrm{ms}} < \hat{\omega}_{\mathrm{er}}$ or $\hat{\omega}_{\mathrm{ms}} > \hat{\omega}_{\mathrm{zd}}$

Here the cases in which the resonance frequency of the metasurface lies outside the bandgap region of the resonant half-space are considered. For example, this can be achieved by using surface and embedded resonators that have identical stiffness but different masses. Fig. 3 shows the dispersion curves for two cases: (a) $\hat{\omega}_{\mathrm{ms}} = 0.5 < \hat{\omega}_{\mathrm{er}}$ and (b) $\hat{\omega}_{\mathrm{ms}} = 1.5 > \hat{\omega}_{\mathrm{zd}}$, where the resonance frequency of the metasurface is below that of the resonant half-space and above the upper edge of the bandgap, respectively. In these cases, the metasurface imposes an extra branch that asymptotically approaches $\hat{\omega}_{\mathrm{ms}}$. This branch is accompanied by an additional narrow bandgap, shown in light green on the dispersion graphs. By shifting the resonance frequency of the metasurfaces towards higher

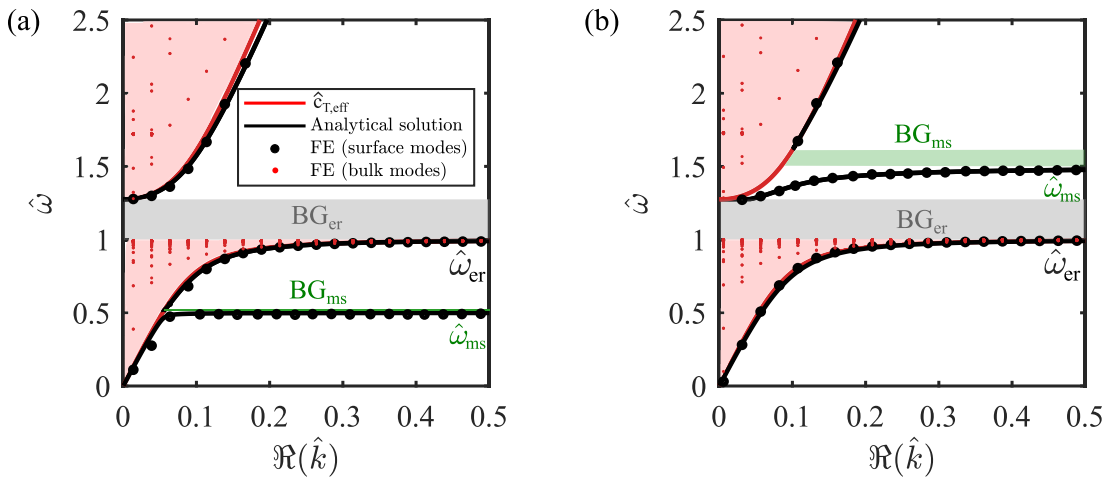

Fig. 3. Dispersion relations for Case II: (a) $\hat{\omega}_{ms} < \hat{\omega}_{er}$ and (b) $\hat{\omega}_{ms} > \hat{\omega}_{zd}$. The highlighted gray and green regions represent the primary and secondary bandgaps associated with the resonant half-space and metasurface, respectively. FE eigensolutions are represented by dots.

values, the metasurface bandgap coefficient B_{ms} in Eq. (10) increases. As a result, the metasurface-induced bandgap frequency range is extended.

Similar to the previous scenario, two FE models are developed, analogous to the one depicted in Fig. 2(a), to validate the analytical results. The comparison between the analytical dispersion curves (solid black lines) and the numerical solutions (black dots) demonstrates good agreement, confirming the accuracy of the proposed analytical model.

3.3. Case III: metasurface resonance frequency inside the half-space bandgap, $\hat{\omega}_{er} < \hat{\omega}_{ms} < \hat{\omega}_{zd}$

This case examines the scenario where the resonance frequency of the metasurface lies within the bandgap of the half-space. In particular, assuming $\hat{M}_{ms} = \hat{M}_{er}$ and $\hat{K}_{ms} = 1.44\,\hat{K}_{er}$, the case $\hat{\omega}_{ms} = 1.2\,\hat{\omega}_{er}$ is considered. The dispersion relation in Fig. 4(a) does not exhibit a secondary bandgap, unlike in the previous cases. Instead, three distinct branches of the surface wave are identified: the lower branch (M1) approaches the resonance frequency of the embedded resonators, $\hat{\omega}_{er}$, while the upper branch (M3) propagates with a velocity constrained between the shear velocity of the homogenized material and the Rayleigh velocity of the host material, i.e., $\hat{c}_{T,\text{eff}} < \hat{c} < \hat{c}_{R,h}$. Additionally, a surface mode (M2) exists within the bandgap of the resonant half-space.

The FE column cell model developed in Fig. 2(a) is used to validate the results of the dispersion analysis and investigate the nature of the existing surface modes. In Fig. 4, the wavefields in terms of vertical displacement for M1, M2 and M3 are shown. These wavefields are obtained by replicating the unit cell eigenmode along the wave propagation direction ($\hat{x}$) with a phase shift $\exp(\mathrm{i}\hat{k}\hat{x})$ over a total length of $\hat{\lambda}_{ref}$, equivalent to 23 column cells. The three modes with normalized wavenumber $\hat{k} = 0.14$ and normalized angular frequencies $\hat{\omega}_{M1} = 0.89$, $\hat{\omega}_{M2} = 1.19$, and $\hat{\omega}_{M3} = 2.09$ are shown in Figs. 4(b–d), corresponding to the lower, localized, and upper branches of the dispersion relation, respectively. Modes M1 and M3 are characterized by in-phase and out-of-phase motions of the embedded resonators and the host medium, respectively, similar to the acoustic and optical branches in any other locally resonant waveguide. These two surface modes marginally interact with the metasurface. Conversely, M2 is highly confined to the surface of the resonant half-space, as a result of the large vertical stresses exchanged between the resonant half-space and the metasurface.

The inset of the dispersion relation (see Fig. 4(e)) focuses on mode M2 around the dimensionless angular frequency ($\hat{\omega}^* = 1.16$). This is the frequency at which mode M2 crosses the fundamental Rayleigh wave in the host material, indicated by the dashed black line in the figure. When surface waves are excited at this frequency in the non-resonant host material, their propagation within the LRM zone is confined to the footprint of the metasurface array, thanks to impedance matching with the host medium, as shown in Fig. 4(f). Note that the localized mode significantly reduces the group velocity of the surface waves, thereby effectively slowing them down.

The group velocity of mode M2 can be slightly adjusted by tuning the metasurface resonance frequency. For $\hat{\omega}_{ms} \to \hat{\omega}_{er}$, the localized M2 branch transitions to a standing mode with nearly zero group velocity, as shown in Fig. 5(a) for $\hat{\omega}_{ms} = 1.02\,\hat{\omega}_{er}$. In contrast, as $\hat{\omega}_{ms} \to \hat{\omega}_{zd}$, a localized mode with a positive group velocity emerges, as shown in Fig. 5(b) for $\hat{\omega}_{ms} = 1.25\,\hat{\omega}_{er}$.

4. Guiding surface waves on structured surfaces

Based on the discussion of Case III, a waveguide problem is analyzed to demonstrate the feasibility of guiding Rayleigh waves in vertical planes. The waveguide, shown in Fig. 6(a), has a length of $\hat{L}_m = 14\hat{\lambda}_{ref}$ and a height $\hat{H}$. It includes a trapezoidal ridge with a height of $\hat{\lambda}_{ref}$, a lower base of $4\hat{\lambda}_{ref}$, and an upper edge of $2\hat{\lambda}_{ref}$, located in the center of the model.

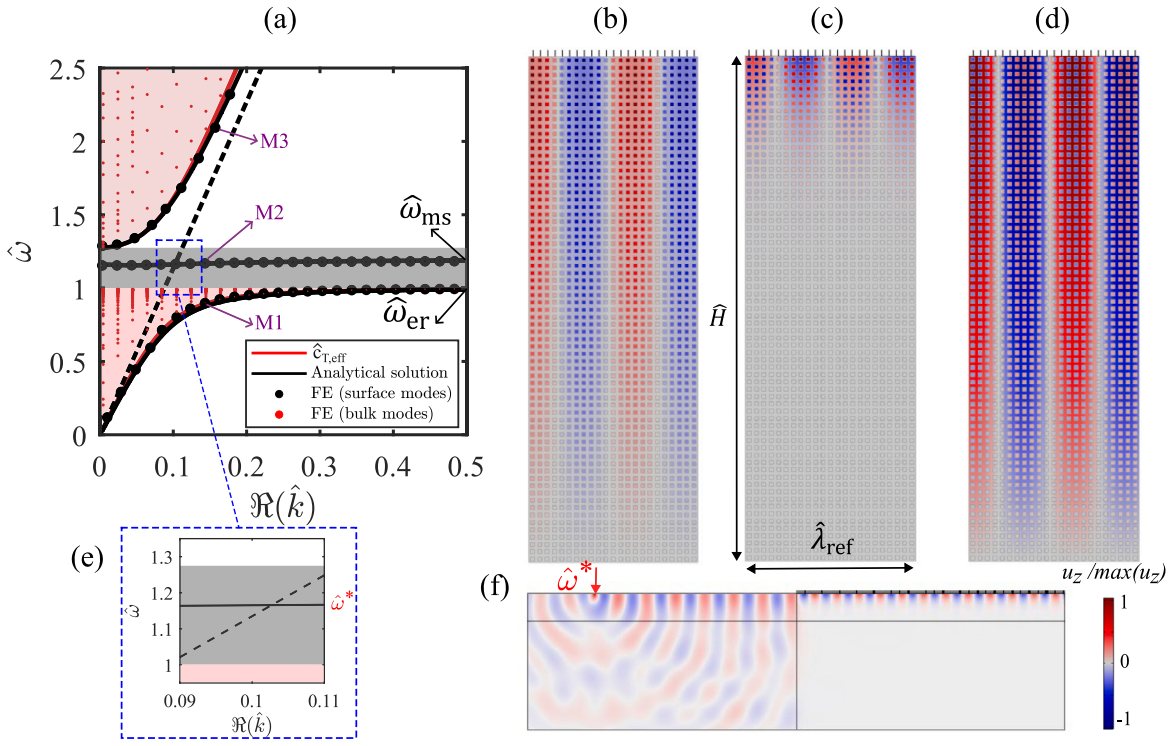

Fig. 4. (a) Dispersion relation for Case III where $\hat{\omega}_{er} < \hat{\omega}_{ms} < \hat{\omega}_{zd}$. The gray region indicates the characteristic bandgap of the resonant half-space. (b-d) Mode shapes of three surface wave branches (M1, M2, and M3) corresponding to $\hat{k} = 0.14$, with frequencies $\hat{\omega}_{M1} = 0.89$, $\hat{\omega}_{M2} = 1.19$, and $\hat{\omega}_{M3} = 2.09$, respectively. (e) The inset figure highlights the frequency matching of the case study with fundamental surface mode of the host material ($\hat{c}_{R,h}$), identified by the dashed black line, at $\hat{\omega}^* = 1.16$. (f) Surface confinement of M2 at $\hat{\omega}^*$.

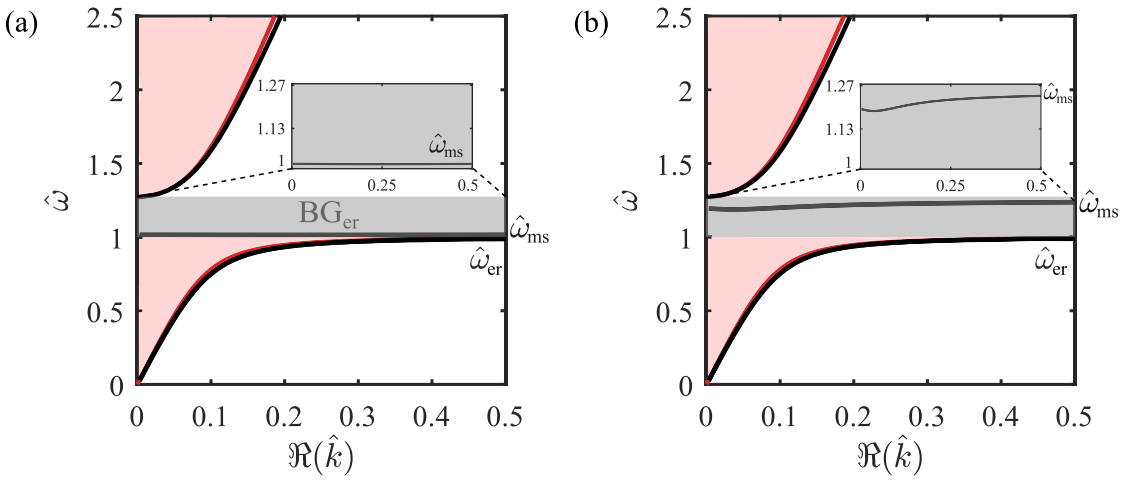

Fig. 5. Dispersion relation for Case III where (a) $\hat{\omega}_{ms} = 1.02\,\hat{\omega}_{er}$, and (b) $\hat{\omega}_{ms} = 1.25\,\hat{\omega}_{er}$. In both figures, the inset panels provide a magnified view of the bandgap region induced by the embedded resonators, highlighting the behavior of the localized mode.

Fig. 6(a) shows the wavefield in terms of the normalized vertical displacement of the reference waveguide, made of an elastic, homogeneous, and isotropic host material. Surface waves are excited at the specific frequency of Case III, $\hat{\omega}^* = 1.16$, with a vertical point source placed at a distance of $\hat{\lambda}_{ref}$ from the model edge. When surface waves impinge on the ridge, phenomena such as (i) back-reflection due to the abrupt change in surface geometry and (ii) scattering at the sharp edges and corners of the trapezoid occur. Consequently, the wavefield is scattered in multiple directions. After passing the perturbed surface, the transmitted surface wave exhibits reduced amplitude, as part of the elastic wave energy is lost through these interactions. Additionally, wave trapping

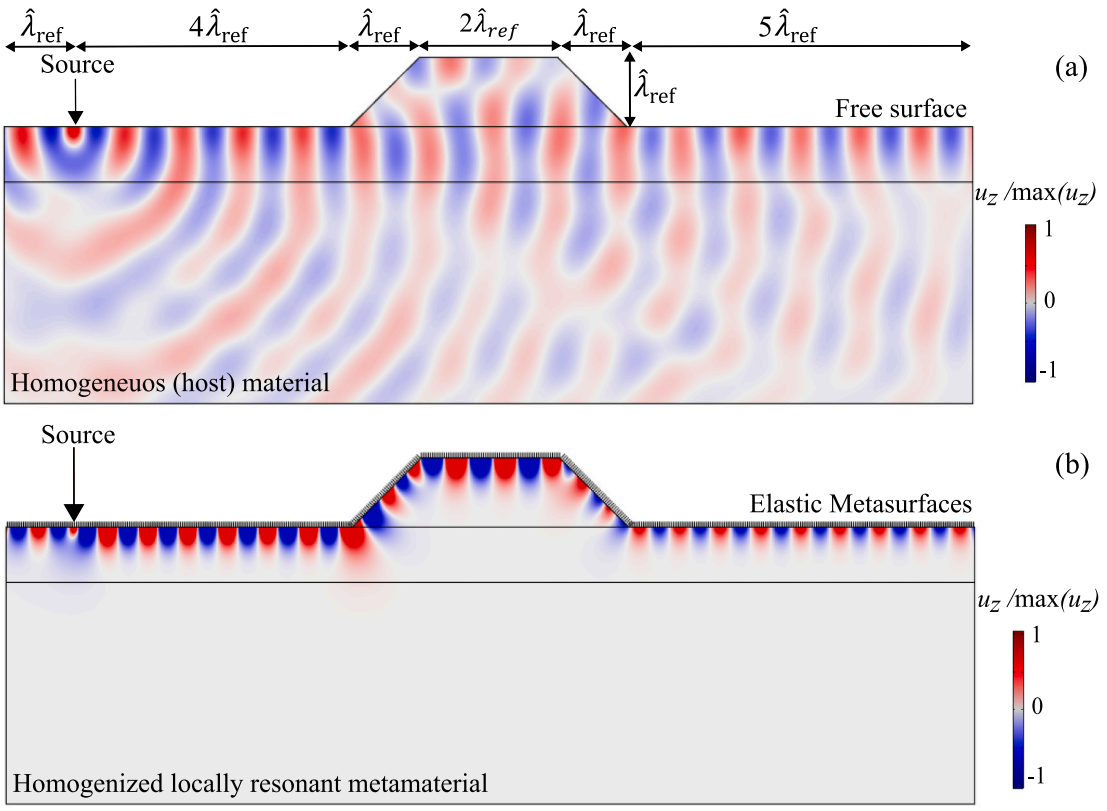

Fig. 6. Surface waves propagating in a waveguide with structured surface geometry in (a) a homogeneous medium and (b) a locally resonant metamaterial decorated with elastic metasurfaces.

may occur within the trapezoidal region, altering the characteristics of the surface wave as it adapts to the new geometry. The extent of these phenomena depends on several factors such as excitation frequency, trapezoid dimensions, and material properties.

Fig. 6(b) shows the same wavefield for the resonant waveguide, where the half-space material is the homogenized LRM, and a metasurface is accommodated at its surface. Following the observation in Case III, the resonance frequency of the metasurface is set to $\hat{\omega}_{\text{ms}} = 1.2\,\hat{\omega}_{\text{er}}$, to support the propagation of the localized M2 mode discussed in Section 3.3. The combined resonant system efficiently guides surface waves along the trapezoidal contour, minimizing energy loss and maintaining wave localization despite geometric irregularities.

Finally, to further demonstrate the wave guiding capability of the proposed methodology, a notch defect is introduced in the center of the domain, as shown in Fig. 7(a). The triangular notch has a length of $\hat{L}_{\text{n}} = 2\,\hat{\lambda}_{\text{ref}}$ and a height $\hat{H}_{\text{n}} = \hat{\lambda}_{\text{ref}}$. The vertical displacement wavefield in Fig. 7(b) demonstrates that surface Rayleigh waves bypass the triangular defect and continue propagating along the waveguide surface with minimal energy loss, even when interacting with sharp angles.

5. Conclusion

In this work, a novel wave guiding approach for Rayleigh waves was introduced, using an elastic metasurface attached to the surface of a resonant half-space. The former consists of a periodic arrangement of mass–spring oscillators, while the latter is formed by embedding multiple rows of periodically distributed mechanical resonators in a host material. By employing a suitable homogenization technique for the resonant half-space and the effective medium approach for the metasurface, both valid under long-wavelength approximation, an analytical closed-form dispersion law was derived. The adopted homogenization technique successfully captures the fundamental dispersive behavior of the resonant system in the frequency range of interest. Although more advanced methods may offer broader validity, especially near resonance or in the presence of spatial heterogeneity, they generally require higher computational cost.

To validate the analytical formulation and evaluate various case studies in different metasurface configurations, FE models were developed. The numerical findings revealed an enhanced filtering property, achieved by extending the bandgap frequency range or creating a secondary bandgap through a proper design of metasurfaces. Notably, a highly confined surface mode emerges when the resonance frequency of the metasurfaces is set within the bandgap of the resonant half-space. This mode effectively guides in-plane surface waves along irregular surfaces. Although a fully homogenized analytical model can be developed for a resonant

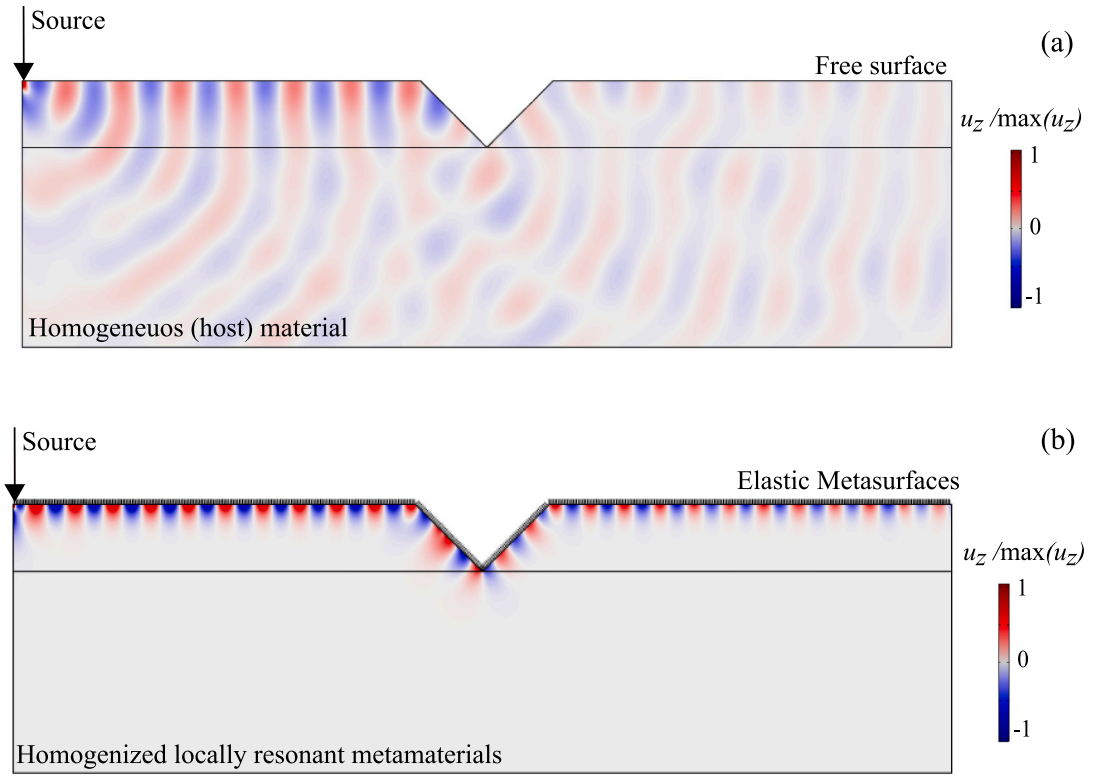

Fig. 7. (a) Propagation of Rayleigh waves in the reference case, where a notch defect remains unaltered, significantly affecting the wavefield. (b) Rayleigh waves guided around the surface defect using a combined resonant system.

bilayer system, in which a thin resonant layer mimics an elastic metasurface placed over a resonant half-space, as demonstrated in Ref. [27], such an approach results in a computationally demanding framework. In contrast, the hybrid strategy proposed in this work significantly reduces the computational burden while preserving sufficient accuracy.

Overall, the analytical and numerical findings of this study contribute to advanced surface wave manipulation across various applications. In ground-borne vibration mitigation systems, locally resonant waveguides can channel train-induced vibrations away from sensitive areas, protecting buildings and delicate electrical equipment. In non-destructive testing, this approach could enable more precise defect detection in materials with irregular surfaces. Furthermore, in surface acoustic wave devices, the proposed methodology could lead to the realization of more efficient and compact sensors, filters, and actuators for telecommunications and signal processing applications.

CRediT authorship contribution statement

Farhad Zeighami: Writing – review & editing, Writing – original draft, Visualization, Software, Resources, Project administration, Methodology, Investigation, Funding acquisition, Formal analysis, Data curation, Conceptualization. **Antonio Palermo:** Writing – review & editing, Validation, Methodology, Conceptualization. **Parisa Shokouhi:** Writing – review & editing, Validation, Methodology, Conceptualization. **Alessandro Marzani:** Writing – review & editing, Validation, Supervision, Methodology, Conceptualization.

Declaration of competing interest

The authors declare that they have no known competing financial interests or personal relationships that could have appeared to influence the work reported in this paper.

Acknowledgments

F.Z. acknowledges the funding received from the Italian Ministry of Education, Universities, and Research (MIUR), Italy for the "ELeMEnT" project (grant agreement SOE0000157, CUP: J53C22003890002), under "Young Researchers Call 2022" of the National Recovery and Resilience Plan (NRRP) funded by the European Union – NextGenerationEU.

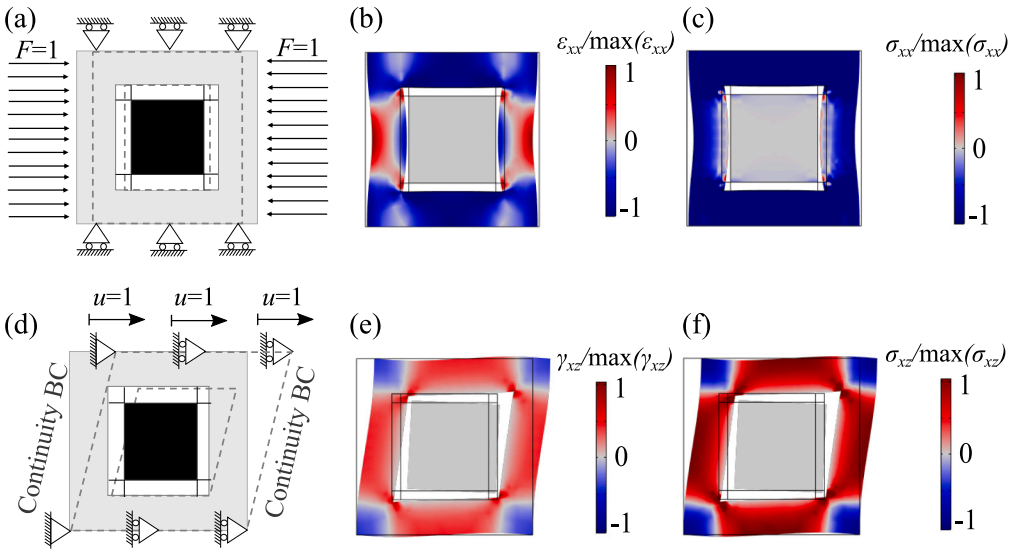

Fig. A.1. (a) Schematic of the unit cell utilized for calculating the effective longitudinal modulus (M_{eff}). Panels (b) and (c) depict numerical FE models employed to compute the normalized strain and stress under a uniaxial constrained deformation state, respectively. Panel (d) Schematic of the unit cell used to determine the effective shear modulus (μ_{eff}). Panels (e) and (f) illustrate numerical FE models used to evaluate the normalized strain and stress under a pure shear deformation state, respectively.

Appendix A. Effective parameters of the resonant half-space

The effective bulk wave velocities of the homogenized resonant half-space ($c_{L,\text{eff}}$ and $c_{T,\text{eff}}$) in Eq. (2) are calculated by evaluating the corresponding effective longitudinal modulus (M_{eff}) and effective shear modulus (μ_{eff}), following the methodology presented in Ref. [27]. For quick reference, relevant equations and information from this study are included in this section. According to the adopted approach, two effective moduli are determined for the reference area of a 2D FE model subjected to constrained uniaxial and shear strain states, as schematically shown in Fig. A.1(a) and (d), respectively, as:

$$M_{\text{eff}} = \frac{\overline{\sigma}_{xx}}{\overline{\varepsilon}_{xx}}, \quad \mu_{\text{eff}} = \frac{\overline{\sigma}_{xz}}{\overline{\gamma}_{xz}}, \tag{A.1}$$

where $\overline{\sigma}_{xx}$ and $\overline{\varepsilon}_{xx}$ denote the mean normal stress and strain components, respectively, associated with the uniaxial constrained deformation of the embedded resonator, restricted to the reference area, S_{er}. Likewise, $\overline{\sigma}_{xz}$ and $\overline{\gamma}_{xz}$ represent the mean shear stress and the corresponding strain component associated with shear deformation, calculated along the top surface (L) of the reference model. These strain and stress quantities are defined as:

$$\overline{\sigma}_{xx} = \frac{\int_{S_{\text{er}}} \sigma_{xx}\, \mathrm{d}S_{\text{er}}}{S_{\text{er}}}, \quad \overline{\varepsilon}_{xx} = \frac{\int_{S_{\text{er}}} \varepsilon_{xx}\, \mathrm{d}S_{\text{er}}}{S_{\text{er}}}, \quad \overline{\sigma}_{xz} = \frac{\int_{L} \sigma_{xz}\, t_{\text{er}}\, \mathrm{d}L}{t_{\text{er}} L}, \quad \overline{\gamma}_{xz} = \frac{\Delta u}{L}, \tag{A.2}$$

where t_{er} denotes the unitary out-of-plane thickness of the model.

To evaluate the effective longitudinal modulus (M_{eff}), unit pressure loads are applied to both lateral edges of the unit cell while restraining its upper and lower boundaries in the vertical direction, as shown schematically in Fig. A.1(a). Fig. A.1(b) and Fig. A.1(c) depict the resulting longitudinal strain and stress distributions normalized by their maximum values inside the unit cell, respectively. By computing the mean stress $\overline{\sigma}_{xx}$ and strain $\overline{\varepsilon}_{xx}$ within the host medium, the effective longitudinal modulus is calculated as $M_{\text{eff}} = \overline{\sigma}_{xx}/\overline{\varepsilon}_{xx} = 36.4$ [MPa].

To determine the effective shear modulus (μ_{eff}), a horizontal unit displacement is applied to the top surface of the unit cell while restraining its lower boundary in the horizontal direction, as shown in Fig. A.1(d). Continuity boundary conditions are imposed along the lateral edges of the unit cell to account for the effects of neighboring cells. Fig. A.1(e) and Fig. A.1(f) show the normalized shear strain and stress distributions, respectively. By calculating the mean shear stress $\overline{\sigma}_{xz}$, the effective shear modulus is estimated as $\mu_{\text{eff}} = \overline{\sigma}_{xz}/\overline{\gamma}_{xz} = 3.6$ [MPa].

The frequency-dependent mass density and bulk wave speeds of the homogenized material, referred to as the effective parameters of the half-space, are numerically determined from Eqs. (1) and (2), respectively. The results reveal a bifurcation in the effective mass density, splitting into two distinct branches with opposite phase responses, as shown in Fig. A.2(a). Below resonance ($\hat{\omega} < 1$), the embedded resonators and the host medium oscillate in the same direction. This results in an effective mass density increase as the additional mass of the resonator contributes to the overall inertia of the system, making it behave like a denser material. In contrast, when $\hat{\omega} > 1$, the embedded resonators and the host media oscillate in opposite directions, resulting in a reduction in

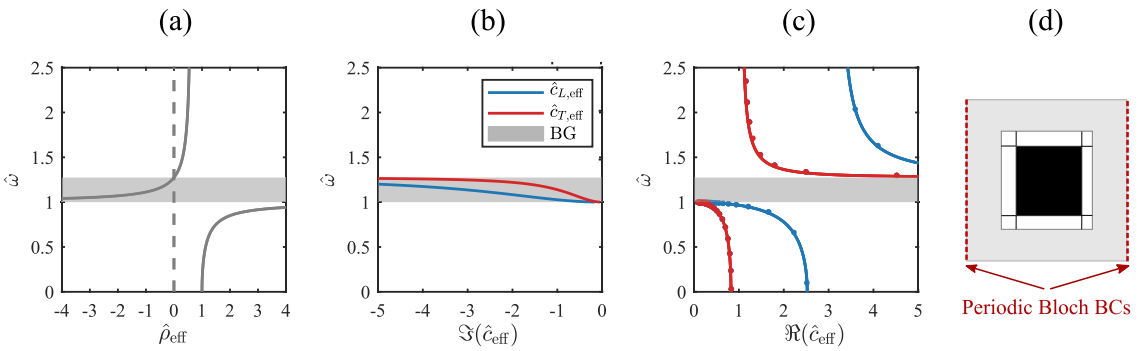

Fig. A.2. (a) Effective mass density of the homogenized LRM. (b) imaginary and (c) real part of the effective bulk wave speeds. Highlighted areas indicate the frequency bandgap of bulk waves. (d) Schematic of the FE model of the unit cell used in direct numerical simulations. The results are over-imposed as dots in panel (c).

the effective mass density [40]. As a result, the effective mass density becomes negative within the frequency range between the resonance frequency of the embedded resonators ($\hat{\omega}_{\text{er}} = 1$) and their zero-density frequency ($\hat{\omega}_{\text{zd}} = 1.27\,\hat{\omega}_{\text{er}}$), where $\hat{\rho}_{\text{eff}}(\hat{\omega}_{\text{zd}}) = 0$. Two limiting values of the mass density are found: $\hat{\rho}_{\text{eff}}(\hat{\omega} = 0) = 1$, which represents the static mass density, and $\hat{\rho}_{\text{eff}}(\hat{\omega} \to +\infty) \to 1 - \rho_0$, which corresponds to the mass density at infinite frequency.

Figs. A.2(b) and (c) display the imaginary and real components of the frequency-dependent bulk wave velocities, calculated from Eq. (2), corresponding to evanescent and propagating bulk waves, respectively. The bulk wave speeds exhibit a bandgap in the frequency range $\hat{\omega}_{\text{BG}} = [1, \hat{\omega}_{\text{zd}}]$, where the effective mass density assumes negative values. The bandgap formation is attributed to the out-of-phase oscillation of the embedded resonators, which interferes with the propagation of bulk waves in the host medium, combined with the periodicity effect of the LRMs. Both bulk waves are attenuated within this bandgap frequency range, as shown in Fig. A.2(b). The real limiting values of the effective wave velocities at zero and infinite frequencies are calculated as:

$$\hat{c}_{L,\text{eff}}(\hat{\omega} = 0) = \sqrt{\frac{\hat{\rho}_{\text{h}} M_{\text{eff}}}{\mu_{\text{h}}}}, \quad \hat{c}_{T,\text{eff}}(\hat{\omega} = 0) = \sqrt{\frac{\hat{\rho}_{\text{h}} \mu_{\text{eff}}}{\mu_{\text{h}}}}, \tag{A.3}$$

$$\hat{c}_{L,\text{eff}}(\hat{\omega} \to +\infty) \to \frac{\hat{c}_{L,\text{eff}}(\hat{\omega} = 0)}{\sqrt{1 - \rho_0}}, \quad \hat{c}_{T,\text{eff}}(\hat{\omega} \to +\infty) \to \frac{\hat{c}_{T,\text{eff}}(\hat{\omega} = 0)}{\sqrt{1 - \rho_0}}. \tag{A.4}$$

To validate the adopted homogenization approach, the numerical solutions computed from a direct numerical simulation are superimposed as dots in Fig. A.2(c). In direct numerical simulations, a 2D numerical FE model of the unit cell is developed. The same mesh types and elements used in Section 3 are employed here to discretize the model. Moreover, periodic Bloch boundary conditions are imposed on the side edges of the basic unit cell to obtain the numerical dispersion relation for bulk waves propagating along the x-direction. The results are generated by sweeping the dimensionless wavenumber within the interval $\hat{k} = [0, 1]$ and calculating the corresponding dimensionless angular frequency. The normalized effective wave velocities are then computed as $\hat{c}_{\text{eff}} = \hat{\omega}/\hat{k}$. As shown in Fig. A.2(c), the agreement between the two approaches confirms the validity of the adopted semi-analytical method.

Appendix B. Design of a graded metasurface for Rayleigh wave conversion and trapping

The configurable design of the elastic metasurfaces enables the realization of graded metasurfaces with variable resonance frequencies, following the design principles of "rainbow trapping" introduced in Ref. [31]. For this purpose, Case I is selected, where the metasurfaces present identical resonance frequencies for the embedded resonators. Hence, two types of graded metasurfaces are considered, one with decreasing and the other with increasing resonance frequencies, as illustrated in Figs. B.1(a) and (b), respectively. The resonance frequencies are tuned by varying the mass of resonators linearly along the metasurface array while keeping their stiffness constant. In both scenarios, the mass and resonance frequency of a single-frequency metasurface, $\hat{M}_{\text{ms}}$ and $\hat{\omega}_{\text{ms}}$, are used to normalize the corresponding values for the graded metasurfaces (hereafter denoted by the subscript gm).

The propagation of surface waves along a graded metasurface with a linearly increasing mass, resulting in a resonance frequency versus resonator position relationship $\hat{\omega}_{\text{gm}}(\hat{x}) \propto \hat{x}^{-1/2}$, is analyzed under harmonic excitation at $\hat{\omega}^* = \hat{\omega}_{\text{ms}}$. Fig. B.1(a) shows the corresponding normalized vertical displacement field. Surface waves propagate without disturbance until they reach the graded metasurface region, where they become increasingly localized because of simultaneous interactions with the embedded resonators and the frequency-varying metasurface. Throughout the array, surface waves propagate exclusively along the lower hybridized branch of the fundamental surface mode in Fig. 2(b). As the mass of the resonators increases moderately, the group velocity of the surface wave decreases progressively until it reaches the location $\hat{x} = 0.5\,\hat{L}_{\text{m}}$, where the wave frequency coincides with the resonance frequency of the graded metasurface and the embedded resonators. At this point, known as the "turning point" in the literature, the surface wave becomes trapped on the surface of the homogenized half-space. Only a negligible portion of the elastic wave energy is transmitted along the array beyond the turning point, primarily localized at the base of the resonators.

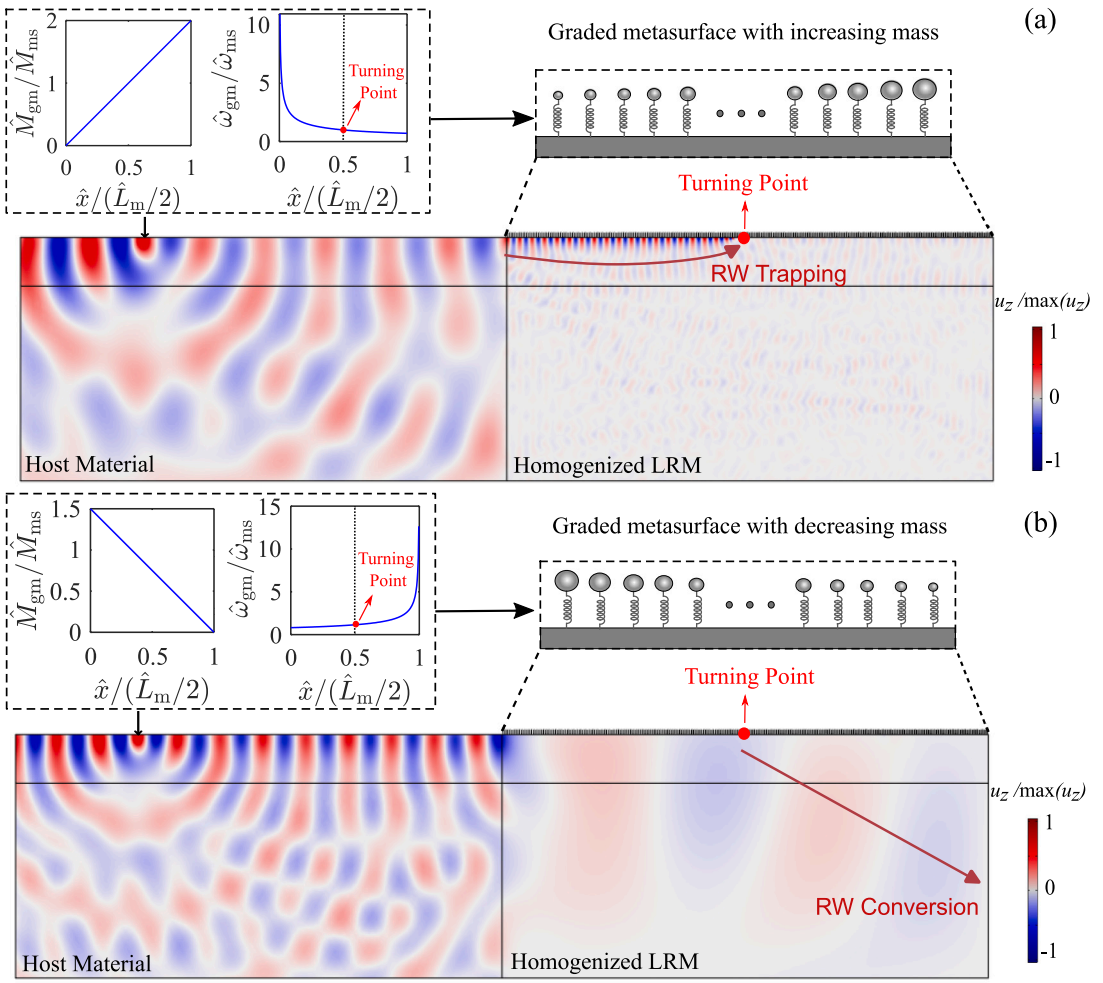

Fig. B.1. (a) The normalized vertical displacement wavefield for graded resonators with linearly increasing mass along the metasurface array, obtained from harmonic excitation at $\hat{\omega}^* = \hat{\omega}_{\mathrm{ms}}$ for Case I. (b) The same quantity for graded resonators with linearly decreasing mass, obtained from harmonic excitation at $\hat{\omega}^* = \hat{\omega}_{\mathrm{BG}_{\mathrm{ms}}}$. The insets depict the variation in mass and resonance frequency of the graded resonators.

In the second scenario, a graded metasurface with a linearly decreasing resonator mass is analyzed under harmonic excitation at $\hat{\omega}^* = \hat{\omega}_{\mathrm{ms}}$. This configuration results in the position-dependent resonance frequency function $\hat{\omega}_{\mathrm{gm}}(\hat{x}) \propto (1-\hat{x})^{-\frac{1}{2}}$, as shown in the inset of Fig. B.1(b). The minimum and maximum values of the mass are intentionally selected such that $\hat{\omega}_{\mathrm{gm}}(0.5\,\hat{L}_{\mathrm{m}}) = \hat{\omega}_{\mathrm{ms}}$. Unlike the previous scenario, here the surface wave propagation along the metasurface array is governed by the upper hybridized branch of the dispersion curve (see Fig. 2(b)). Due to the spatially variable resonance frequency, the mode gradually transitions from a surface-localized state to a bulk-like state, reaching the turning point at $\hat{x} = 0.5\,\hat{L}_{\mathrm{m}}$. At this point, the wave frequency coincides with the upper branch cut-on frequency, marking the conversion into a bulk shear wave propagating with phase velocity $\hat{c}_{\mathrm{RW}} = \hat{c}_{T,\mathrm{eff}}$, characterized by a corresponding longer wavelength.

Data availability

Data will be made available on request.

References

[1] L. Rayleigh, On waves propagated along the plane surface of an elastic solid, Proc. Lond. Math. Soc. s1-17 (1) (1885) 4–11, http://dx.doi.org/10.1112/plms/s1-17.1.4.

[2] E.A. Ash, E.G.S. Paige (Eds.), Rayleigh-wave theory and application, in: Springer Series on Wave Phenomena, vol. 1, Springer Berlin, Heidelberg, 1985, p. X, 362, http://dx.doi.org/10.1007/978-3-642-82621-4.

[3] M.M. Sigalas, E.N. Economou, Elastic and acoustic wave band structure, J. Sound Vib. 158 (2) (1992) 377–382, http://dx.doi.org/10.1016/0022-460X(92)90059-7.

[4] M.S. Kushwaha, P. Halevi, L. Dobrzynski, B. Djafari-Rouhani, Acoustic band structure of periodic elastic composites, Phys. Rev. Lett. 71 (13) (1993) 2022–2025, http://dx.doi.org/10.1103/PhysRevLett.71.2022.

[5] Z. Liu, X. Zhang, Y. Mao, Y.Y. Zhu, Z. Yang, C.T. Chan, P. Sheng, Locally resonant sonic materials, Science 289 (5485) (2000) 1734–1736, http://dx.doi.org/10.1126/science.289.5485.1734.

[6] N.X. Fang, D. Xi, J. Xu, M.S. Ambati, W. Srituravanich, C. Sun, X. Zhang, Ultrasonic metamaterials with negative modulus, Nat. Mater. 5 (2006) 452–456, http://dx.doi.org/10.1038/nmat1644.

[7] Y. Ding, Z. Liu, C. Qiu, J. Shi, Metamaterial with simultaneously negative bulk modulus and mass density, Phys. Rev. Lett. 99 (9) (2007) 093904, http://dx.doi.org/10.1103/PhysRevLett.99.093904.

[8] C. Yilmaz, G.M. Hulbert, N. Kikuchi, Phononic band gaps induced by inertial amplification in periodic media, Phys. Rev. B 76 (5) (2007) 054309, http://dx.doi.org/10.1103/PhysRevB.76.054309.

[9] D. Mu, H. Shu, L. Zhao, S. An, A review of research on seismic metamaterials, Adv. Eng. Mater. 22 (4) (2020) 1901148, http://dx.doi.org/10.1002/adem.201901148.

[10] P. Jiao, J. Mueller, J.R. Raney, X.R. Zheng, A.H. Alavi, Mechanical metamaterials and beyond, Nat. Commun. 14 (6004) (2023) http://dx.doi.org/10.1038/s41467-023-41679-8.

[11] A. Palermo, S. Krödel, A. Marzani, C. Daraio, Engineered metabarrier as shield from seismic surface waves, Sci. Rep. 6 (2016) 39356, http://dx.doi.org/10.1038/srep39356.

[12] J.-J. Marigo, K. Pham, A. Maurel, S. Guenneau, Effective model for elastic waves propagating in a substrate supporting a dense array of plates/beams with flexural resonances, J. Mech. Phys. Solids 143 (2020) 104029, http://dx.doi.org/10.1016/j.jmps.2020.104029.

[13] L.S.S. Pillarisetti, C.J. Lissenden, P. Shokouhi, Control of Rayleigh wave propagation through imposing Mindlin boundary conditions on the surface, J. Sound Vib. 530 (2022) 116931, http://dx.doi.org/10.1016/j.jsv.2022.116931.

[14] D.J. Colquitt, A. Colombi, R.V. Craster, P. Roux, S.R.L. Guenneau, Seismic metasurfaces: Sub-wavelength resonators and Rayleigh wave interaction, J. Mech. Phys. Solids 99 (2017) 379–393, http://dx.doi.org/10.1016/j.jmps.2016.12.004.

[15] L.S.S. Pillarisetti, C.J. Lissenden, P. Shokouhi, Partially embedded metabarrier to suppress surface waves in granular media, J. Acoust. Soc. Am. 156 (3) (2024) 1594–1608, http://dx.doi.org/10.1121/10.0028536.

[16] N. Boechler, J.K. Eliason, A. Kumar, A.A. Maznev, K.A. Nelson, N. Fang, Interaction of a contact resonance of microspheres with surface acoustic waves, Phys. Rev. Lett. 111 (3) (2013) 036103, http://dx.doi.org/10.1103/PhysRevLett.111.036103.

[17] A. Colombi, P. Roux, S. Guenneau, P. Gueguen, R.V. Craster, Forests as a natural seismic metamaterial: Rayleigh wave bandgaps induced by local resonances, Sci. Rep. 6 (2016) 19238, http://dx.doi.org/10.1038/srep19238.

[18] F. Zeighami, L. Sandoval, A. Guadagnini, V. Di Federico, Uncertainty quantification and global sensitivity analysis of seismic metabarriers, Eng. Struct. 277 (2023) 115415, http://dx.doi.org/10.1016/j.engstruct.2022.115415.

[19] A.F. Russillo, F. Arena, G. Failla, Water-tank metabarrier for seismic Rayleigh wave attenuation, Philos. Trans. R. Soc. A 382 (2279) (2024) 20230363, http://dx.doi.org/10.1098/rsta.2023.0363.

[20] Y. Ni, Z. Shi, Surface wave mitigation by periodic wave barriers under a moving load: Theoretical analysis, numerical simulation and experimental validation, Philos. Trans. R. Soc. A 382 (2278) (2024) 20240020, http://dx.doi.org/10.1098/rsta.2024.0020.

[21] F. Nistri, F. Bosia, A.S. Gliozzi, L. D'Alessandro, S. Caverni, P. Charkaluk, A. Corigliano, M. Miniaci, A. Colombi, N.M. Pugno, Design and in field validation of a modular metamaterial for mitigation of railway induced vibrations, Soil Dyn. Earthq. Eng. 180 (2024) 108594, http://dx.doi.org/10.1016/j.soildyn.2024.108594.

[22] J.M. De Ponti, A. Colombi, E. Riva, R. Ardito, F. Braghin, A. Corigliano, R.V. Craster, Experimental investigation of amplification, via a mechanical delay-line, in a rainbow-based metamaterial for energy harvesting, Appl. Phys. Lett. 117 (14) (2020) 143902, http://dx.doi.org/10.1063/5.0023544.

[23] G.J. Chaplain, J.M. De Ponti, G. Aguzzi, A. Colombi, R.V. Craster, Topological rainbow trapping for elastic energy harvesting in graded Su–Schrieffer–Heeger systems, Phys. Rev. Appl. 14 (5) (2020) 054035, http://dx.doi.org/10.1103/PhysRevApplied.14.054035.

[24] A. Colombi, V. Ageeva, R. Smith, A. Clare, R. Patel, M. Clark, D. Colquitt, P. Roux, S. Guenneau, R. Craster, Enhanced sensing and conversion of ultrasonic Rayleigh waves by elastic metasurfaces, Sci. Rep. 7 (2017) http://dx.doi.org/10.1038/s41598-017-07151-6.

[25] F. Zeighami, S. Quqa, J.M. De Ponti, N. Ayyash, A. Marzani, A. Palermo, Elastic metasurfaces for Scholte–Stoneley wave control, Philos. Trans. R. Soc. A 382 (2278) (2024) 20230365, http://dx.doi.org/10.1098/rsta.2023.0365.

[26] B. Assouar, B. Liang, Y. Wu, Y. Li, J.-C. Cheng, Y. Jing, Acoustic metasurfaces, Nat. Rev. Mater. 3 (2018) 460–472, http://dx.doi.org/10.1038/s41578-018-0061-4.

[27] F. Zeighami, A. Palermo, A. Marzani, Rayleigh waves in locally resonant metamaterials, Int. J. Mech. Sci. 195 (2021) 106250, http://dx.doi.org/10.1016/j.ijmecsci.2020.106250.

[28] F. Zeighami, A. Palermo, D. Bogomolov, A. Marzani, Experimental investigation of Rayleigh wave propagation in a locally resonant metamaterial layer resting on an elastic half-space, APL Mater. 12 (2) (2024) 021115, http://dx.doi.org/10.1063/5.0171532.

[29] S.D.M. Adams, R.V. Craster, D.P. Williams, Rayleigh waves guided by topography, Proc. R. Soc. A 463 (2078) (2007) 531–550, http://dx.doi.org/10.1098/rspa.2006.1779.

[30] N. Aravantinos-Zafiris, K.A. Chondrogiannis, H.R. Thomsen, V.K. Dertimanis, A. Colombi, M.M. Sigalas, E. Chatzi, Terraced slope metasurface in granular media, Geophys. J. Int. 238 (1) (2024) 43–52, http://dx.doi.org/10.1093/gji/ggae150.

[31] A. Colombi, S. Guenneau, P. Roux, R.V. Craster, Transformation seismology: Composite soil lenses for steering surface elastic Rayleigh waves, Sci. Rep. 6 (2016) 25320, http://dx.doi.org/10.1038/srep25320.

[32] Z. Chatzopoulos, A. Palermo, A. Diatta, S. Guenneau, A. Marzani, Cloaking Rayleigh waves via symmetrized elastic tensors, Internat. J. Engrg. Sci. 191 (2023) 103899, http://dx.doi.org/10.1016/j.ijengsci.2023.103899.

[33] A.A. Maznev, V.E. Gusev, Waveguiding by a locally resonant metasurface, Phys. Rev. B 92 (11) (2015) 115422, http://dx.doi.org/10.1103/PhysRevB.92.115422.

[34] H.H. Huang, C.T. Sun, G.L. Huang, On the negative effective mass density in acoustic metamaterials, Internat. J. Engrg. Sci. 47 (4) (2009) 610–617, http://dx.doi.org/10.1016/j.ijengsci.2008.12.007.

[35] K.F. Graff, Wave motion in elastic solids, in: Dover Books on Physics, Dover, New York, NY, 1991.

[36] E.A. Garova, A.A. Maradudin, A.P. Mayer, Interaction of Rayleigh waves with randomly distributed oscillators on the surface, Phys. Rev. B 59 (20) (1999) 13291–13296, http://dx.doi.org/10.1103/PhysRevB.59.13291.

[37] Comsol Multiphysics®, COMSOL AB, stockholm, Sweden, 2025, URL https://www.comsol.com.

[38] B.R. Mace, E. Manconi, Modelling wave propagation in two-dimensional structures using finite element analysis, J. Sound Vib. 318 (4) (2008) 884–902, http://dx.doi.org/10.1016/j.jsv.2008.04.039.

[39] A. Palermo, M. Vitali, A. Marzani, Metabarriers with multi-mass locally resonating units for broad band Rayleigh waves attenuation, Soil Dyn. Earthq. Eng. 113 (2018) 265–277, http://dx.doi.org/10.1016/j.soildyn.2018.05.035.

[40] P. Sheng, J. Mei, Z. Liu, W. Wen, Dynamic mass density and acoustic metamaterials, Phys. B: Condens. Matter 394 (2) (2007) 256–261, http://dx.doi.org/10.1016/j.physb.2006.12.046.